

---

# Conditional Diffusion Models for Uncertainty Estimation in Super Resolution Microscopy

---

Anonymous Author(s)

Affiliation

Address

email

## Abstract

1 Deep learning has recently attracted considerable attention from researchers in  
2 the natural sciences, particularly microscopists, for fast extraction of physically  
3 relevant information from images. However, simple and interpretable uncertainty  
4 quantification is lacking in these applications, and remains a necessary modeling  
5 component in high-risk research. In order to quantify uncertainty in otherwise  
6 deterministic image translation architectures, we propose a hybrid generative  
7 modeling framework based on denoising diffusion probabilistic models (DDPMs).  
8 Specifically, our model combines a deterministic neural network with a DDPM,  
9 which can improve conditional synthesis speed and fidelity of the DDPM, while  
10 providing a natural mechanism for uncertainty estimation via Langevin dynamics.  
11 We apply our model to the task of single molecule localization in fluorescence  
12 microscopy, and demonstrate that blending the DeepSTORM architecture with  
13 a DDPM permits simultaneous high-fidelity super-resolution with uncertainty  
14 estimation of kernel density estimates (KDEs) regressed by DeepSTORM. Our  
15 results suggest the proposed solution is an interesting addition to the modeling  
16 toolkit for fluorescence microscopists and the field of deep image translation in  
17 general.

## 18 1 Introduction

19 Deep learning has attracted tremendous attention from researchers in the natural sciences, with  
20 several foundational applications arising in microscopy, e.g., (Weigert 2018; Falk 2019). Recently,  
21 the application of deep image translation in single-molecule localization microscopy (SMLM) has  
22 received considerable interest (Ouyang 2018; Nehme 2020; Speiser 2021). SMLM techniques  
23 are a mainstay of fluorescence microscopy and can be used to produce a pointillist representation  
24 of biomolecules in the cell at diffraction-unlimited precision (Rust 2006; Betzig 2006). As this  
25 technology enables increasingly precise measurements of the cellular environment, there is an  
26 increasing need for machine learning methods to report uncertainty for quality control.

27 In previous applications of deep models to localization microscopy, super-resolution images can be  
28 recovered from a sparse set of localizations with conditional generative adversarial networks (Ouyang  
29 2018) or kernel density estimation can be performed using convolutional networks (Nehme 2020;  
30 Speiser 2021). Here, we focus on the latter class of models which perform single molecule localization  
31 using neural networks. In this approach, one estimates molecular coordinates by predicting kernel  
32 density estimates (KDEs)  $y$ , which are latent in the raw data  $x$ , using a convolutional neural network.  
33 Importantly, inferences in SMLM are often necessarily made on a single measurement, thus common  
34 measures of model performance are based on localization errors computed over ensembles of  
35 simulated images. However, this choice precludes computation of aleatoric uncertainty at test time  
36 under a fixed model, and may result in the application of models to out of distribution datasets.



Figure 1: Generative model of single molecule localization microscopy images

Bayesian probability theory offers us mathematically grounded tools to reason about model uncertainty, but these usually come with a prohibitive computational cost (Gal 2022). A few approaches to avoiding this intractability in deep models have been deterministic uncertainty quantification (Amersfoort 2020), ensembling (Lakshminarayanan et al., 2017) or Monte Carlo dropout (Gal and Ghahramani, 2016). Here, we report a method which models estimates uncertainty in KDE predictions by combining deterministic deep learning with deep generative modeling in a hybrid algorithm. Our approach produces pixel-wise uncertainties in model predictions with no modification to the existing architecture, and can be used for downstream filtering of erroneous image regions. We choose to model a distribution on high-resolution KDE predictions, conditioned on a low-resolution input, using a denoising diffusion probabilistic model (DDPM) (Ho 2020), referred to here as simply “diffusion model”. Such models are well suited conditional image generation tasks, demonstrating promising results in detail reconstruction, while directly providing a mechanism for uncertainty estimation in model predictions (Saharia 2021). Our approach could be readily integrated with existing localization performance measures to address both model accuracy on training data and precision on datasets produced by experiments.

## 2 Background

### 2.1 Image Likelihood and Localization Error

The central objective of single molecule localization microscopy is to infer a set of molecular coordinates  $\theta$  from measured low resolution images  $\mathbf{x}$ . The likelihood on a particular pixel  $k$ , i.e.,  $p(\mathbf{x}_k|\theta)$  is taken to be a convolution of Poisson and Gaussian distributions, due to shot noise  $p(s_k) = \text{Poisson}(\omega_k)$  and sensor readout noise  $p(\zeta_k) = \mathcal{N}(o_k, \sigma_k^2)$

$$p(\mathbf{x}_k|\theta) = A \sum_{q=0}^{\infty} \frac{1}{q!} e^{-\omega_k} \omega_k^q \frac{1}{\sqrt{2\pi}\sigma_k} e^{-\frac{(\mathbf{x}_k - g_k q - o_k)^2}{2\sigma_k^2}} \approx \text{Poisson}(\omega'_k) \quad (1)$$

where  $A$  is some normalization constant and  $\omega'_k = \omega_k + \sigma_k^2$ . For the sake of generality, we include a per-pixel gain factor  $g_k$ , which is often unity. In practice, the summation in (1) can be difficult to work with, and it is common to instead use a Poisson-Normal approximation for simplification, valid under a range of experimental conditions (Huang 2013). This result can be seen from the fact the the convolution of two Poisson distributions is also Poisson. The expectation of the Poisson process at each pixel of the image is computed from the optical transfer function  $O(u, v)$ , which is often a two-dimensional isotropic Gaussian.

$$\omega = i_0 \int O(u) du \int O(v) dv \quad (2)$$

The above integration can be carried out by computing differences of error functions, as detailed in Appendix A. The complete generative process is depicted in Figure 1.

Reliable estimation of  $\theta$  from  $\mathbf{x}$ , for example by maximum likelihood estimation or with a deep model, requires performance metrics for model selection. We use the Fisher information as an information theoretic criteria to assess the quality of the model tested here, with respect to the root mean squared error (RMSE) of our predictions of  $\theta$  (Chao 2016). The Poisson log-likelihood  $\ell(\mathbf{x}|\theta)$  is also convenient for computing the Fisher information matrix (Smith 2010) and thus the Cramer-Rao lower bound, which bounds the variance of a statistical estimator of  $\theta$ , from below

73 i.e.,  $\text{var}(\hat{\theta}) \geq I^{-1}(\theta)$ . The Fisher information is straightforward to compute under the Poisson  
 74 log-likelihood, which is detailed in the Appendix

$$\mathcal{I}_{ij}(\theta) = \mathbb{E}_{\theta} \left( \frac{\partial \ell}{\partial \theta_i} \frac{\partial \ell}{\partial \theta_j} \right) = \sum_k \frac{1}{\omega'_k} \frac{\partial \omega'_k}{\partial \theta_i} \frac{\partial \omega'_k}{\partial \theta_j} \quad (3)$$

## 75 2.2 Kernel density estimation with deep networks

76 Direct optimization of the likelihood in (1) from observations  $\mathbf{x}$  alone is challenging when fluorescent  
 77 emitters are dense within the field of view and fluorescent signals significantly overlap. However, con-  
 78 volutional neural networks (CNN) have recently proven to be powerful tools fluorescence microscopy  
 79 to extract parameters describing fluorescent emitters such as color, emitter orientation,  $z$ -coordinate,  
 80 and background signal (Zhang 2018; Kim 2019; Zelger 2018). For localization tasks, CNNs typically  
 81 employ upsampling layers to reconstruct Bernoulli probabilities of emitter occupancy (Speiser 2021)  
 82 or kernel density estimates with higher resolution than experimental measurements (Nehme 2020).  
 83 Kernel density estimates, denoted by  $\mathbf{y}$ , are the most common data structure used in SMLM, and can  
 84 be easily generated from molecular coordinates, alongside observations  $\mathbf{x}$ , using well-understood  
 85 models of the optical impulse response (Zhang 2007).

## 86 3 Conditional Diffusion for Uncertainty-Aware Super Resolution

87 We consider datasets  $(\mathbf{x}_i, \mathbf{y}_i, \hat{\mathbf{y}}_i)_{i=1}^N$  of observed images  $\mathbf{x}_i$  true kernel density estimate (KDE) images  
 88  $\mathbf{y}_i$ , and KDE estimates  $\hat{\mathbf{y}}_i = \phi(\mathbf{x}_i)$ . Observations  $\mathbf{x}_i$  are simulated under the Poisson likelihood (1)  
 89 and KDEs are generated using (2) alone, followed by appropriate normalization.

### 90 3.1 Problem Statement

91 Point estimates  $\hat{\mathbf{y}}_i$  produced by the traditional deep architectures for super resolution microscopy  
 92 produce strong results, but lack uncertainty quantification. Recent advances in generative modeling,  
 93 particularly DDPMs, therefore present a unique opportunity to integrate uncertainty awareness into the  
 94 super-resolution microscopy toolkit. However, sampling from DDPMs is computationally expensive,  
 95 given that generation amounts to solving a complex stochastic differential equation, effectively  
 96 mapping a simple base distribution to the complex data distribution. The solution of such equations  
 97 requires numerical integration with very small step sizes, resulting in thousands of neural network  
 98 evaluations (Saharia 2021; Vahdat 2021). Furthermore, for conditional generation tasks in high-risk  
 99 applications, generation complexity is further exacerbated by the need for the highest level of detail  
 100 in generated samples.

101 Under these considerations, we propose that DDPM sampling is preceded by a deterministic trans-  
 102 formation  $\phi$ , trained to predict  $\mathbf{y}$  from  $\mathbf{x}$ . Reasoning for this choice in the current application is  
 103 two-fold:

104 **Synthesis Speed.** By training a preprocessor  $\phi$  to obtain an approximate estimate of  $\mathbf{y}$ , we can  
 105 reduce the number of iterations, since the DDPM only needs to model the remaining mismatch,  
 106 resulting in a less complex model from which sampling becomes easier. This approach is  
 107 analogous to latent score-based generative models (LSGMs) discussed in (Vahdat 2021). Speed is  
 108 critical in SMLM applications, which can produce large volumes of image data in a single experiment.  
 109

110 **Sample Fidelity.** Since Langevin dynamics will often be initialized in low-density regions of the data  
 111 distribution, inaccurate score estimation in these regions will negatively affect the sampling process  
 112 (Song 2019). Moreover, mixing can be difficult because of the need of traversing low density regions  
 113 to transition between modes of the distribution. Preprocessing with a deterministic mapping  $\phi$  can  
 114 ameliorate this issue, by eliminating the need for score estimation in low density regions.

115 The preprocessor  $\phi$  is realized by a CNN with upsampling layers that transforms  $\mathbf{x}$  from a low  
 116 dimensional space to a higher one with the same dimension as  $\mathbf{y}$ . Consider the Markov chain wherein  
 117 the KDE  $\mathbf{y}$  is latent in and inferred from a noisy measurement  $\mathbf{x}$ , i.e.,  $\mathbf{x} \rightarrow \phi(\mathbf{x}) \rightarrow \hat{\mathbf{y}}$ . By the  
 118 data processing inequality the function  $\phi$  can only destroy information in  $\mathbf{x}$  pertaining to  $\mathbf{y}$  i.e.,  
 119  $I(\mathbf{x}; \mathbf{y}) \geq I(\phi(\mathbf{x}); \mathbf{y})$  or  $h(\mathbf{y}|\phi(\mathbf{x})) \geq h(\mathbf{y}|\mathbf{x})$  where  $I$  is the mutual information and  $h$  is the entropy.

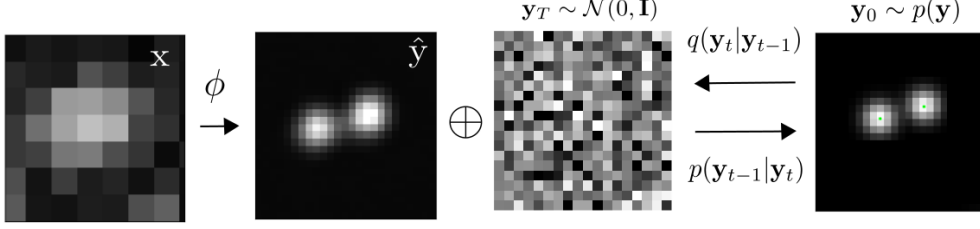


Figure 2: Conditional diffusion model for sampling kernel density estimates

In other words, the function  $\phi$ , while deterministic, can introduce additional uncertainty about  $\mathbf{y}$  in downstream stochastic models by destroying information. Here, we are interested in measuring the upper bound  $h(\mathbf{y}|\phi(\mathbf{x}))$ , as this is the relevant quantity when a deterministic transformation  $\phi$  is an unavoidable first step.

In practice, a DDPM  $\Psi$  can be trained on pairs  $(\mathbf{y}_i, \hat{\mathbf{y}}_i)_{i=1}^N$ . The conditional DDPM generates a target KDE  $\mathbf{y}_0$  in  $T$  refinement steps. Starting with a pure noise image  $\mathbf{y}_T \sim \mathcal{N}(0, \mathbf{I})$ , the model iteratively refines the KDE through successive iterations according to learned conditional transition distributions  $p(\mathbf{y}_{t-1}|\mathbf{y}_t)$  such that  $\mathbf{y}_0 \sim p(\mathbf{y}|\hat{\mathbf{y}})$

### 3.2 Gaussian Diffusion

Diffusion models (Sohl-Dickstein 2015; Ho 2020) are a class of generative models inspired by nonequilibrium statistical physics, which slowly destroy structure in a data distribution  $p(\mathbf{y}_0|\mathbf{x})$  via a fixed Markov chain referred to as the *forward process*. In the present context, the forward process gradually adds Gaussian noise to the KDE  $\mathbf{y}$  according to a variance schedule  $\beta_{0:T}$

$$q(\mathbf{y}_t|\mathbf{y}_0) = \prod_{t=1}^T q(\mathbf{y}_t|\mathbf{y}_{t-1}) \quad q(\mathbf{y}_t|\mathbf{y}_{t-1}) = \mathcal{N}\left(\sqrt{1-\beta_t}\mathbf{y}_{t-1}, \beta_t \mathbf{I}\right) \quad (4)$$

An important property of the forward process is that it admits sampling  $\mathbf{y}_t$  at an arbitrary timestep  $t$  in closed form (Ho 2020). Using the notation  $\alpha_t := 1 - \beta_t$  and  $\gamma_t := \prod_{s=1}^t \alpha_s$ , we have

$$q(\mathbf{y}_t|\mathbf{y}_0) = \mathcal{N}\left(\sqrt{\gamma_t}\mathbf{y}_0, (1-\gamma_t)\mathbf{I}\right) \quad (5)$$

The usual procedure is then to learn a parametric representation of the *reverse process*, and therefore generate samples from  $p(\mathbf{y}_0)$ , starting from noise. Formally,  $p_\theta(\mathbf{y}_0|\hat{\mathbf{y}}) = \int p_\theta(\mathbf{y}_{0:T}|\hat{\mathbf{y}})d\hat{\mathbf{y}}_{1:T}$  where  $\mathbf{y}_t$  is a latent representation with the same dimensionality of the data.  $p_\theta(\mathbf{y}_{0:T}|\hat{\mathbf{y}})$  is a Markov process, starting from a noise sample  $p_\theta(\mathbf{y}_T) = \mathcal{N}(0, \mathbf{I})$ .

$$p_\theta(\mathbf{y}_{0:T}) = p_\theta(\mathbf{y}_T) \prod_{t=1}^T p_\theta(\mathbf{y}_{t-1}|\mathbf{y}_t) \quad p_\theta(\mathbf{y}_{t-1}|\mathbf{y}_t) = \mathcal{N}(\mu_\theta(\mathbf{y}_t), \beta_t \mathbf{I}) \quad (6)$$

where we reuse the variance schedule of the forward process (Ho 2020). We seek to learn a denoising model  $\mu_\theta$  which computes the mean of the Gaussian transition density at each time step  $t$ . For all  $t > 0$ , the mean of the transition density is computed as

$$\mu_\theta(\mathbf{y}_t, \hat{\mathbf{y}}, \gamma_t) = \frac{1}{\sqrt{\alpha_t}} \left( \mathbf{y}_t - \frac{(1-\alpha_t)}{\sqrt{1-\gamma_t}} f_\theta(\mathbf{y}, \hat{\mathbf{y}}, \gamma_t) \right) \quad (7)$$

where  $f_\theta$  is a neural network. Only at  $t = 0$  is this mean directly a function of  $\mathbf{x}$ .

### 143 3.3 Optimization of the Denoising Model

144 To reverse the diffusion process, we optimize a neural denoising model  $f_\theta$  that takes as input  $\hat{\mathbf{y}}$  and a  
 145 noisy target image  $\mathbf{y}_t \sim q(\mathbf{y}_t|\mathbf{y}_0)$ . That is, this noisy target image  $\mathbf{y}_t$  is drawn from the marginal  
 146 distribution of noisy images at a time step  $t$  of the forward diffusion process.

$$\mathbf{y}_t = \sqrt{\gamma}\mathbf{y}_0 + \sqrt{1-\gamma}\epsilon, \quad \epsilon \sim \mathcal{N}(0, \mathbf{I}) \quad (8)$$

147 In addition to a source image  $\mathbf{y}_0$  and a noisy target image  $\mathbf{y}_t$ , the denoising model  $f_\theta$  takes as input  
 148 the sufficient statistics for the variance of the noise  $\gamma$ , and is trained to predict the noise vector  $\epsilon$ .  
 149 We make the denoising model aware of the level of noise through conditioning on a scalar  $\gamma$ . The  
 150 proposed objective function for training  $f_\theta$  is

$$\mathbb{E}_{(\hat{\mathbf{y}}, \mathbf{y}_0)} \mathbb{E}_{(\epsilon, \gamma)} \left[ f_\theta \left( x, \sqrt{\gamma}\mathbf{y}_0 + \sqrt{1-\gamma}\epsilon \mid \mathbf{y}_t, \gamma \right) - \epsilon \right], \quad (9)$$

151 where  $(\hat{\mathbf{y}}, \mathbf{y}_0)$  is sampled from the training dataset and  $\gamma \sim p(\gamma)$ . The distribution of  $\gamma$  has a big  
 152 impact on the quality of the model and the generated outputs. For our training noise schedule, we  
 153 use a piecewise distribution for  $\gamma$ ,  $p(\gamma) = \frac{1}{T} \sum_{t=1}^T U(\gamma_{t-1}, \gamma_t)$  (Nanxin 2021). Specifically, during  
 154 training, we first uniformly sample a time step  $t \sim \{0, \dots, T\}$  followed by sampling  $\gamma \sim U(\gamma_{t-1}, \gamma_t)$ .  
 155 We set  $T = 100$  in all our experiments.

### 156 3.4 Optimization of the DeepSTORM architecture

157 A first pass at localization treats localization as a binary classification problem, such that 0 denotes  
 158 a vacant pixel and 1 denotes an occupied pixel containing an emitter. Direct learning of pixel-wise  
 159 classification with cross-entropy loss leads to an imbalance of occupied and unoccupied pixels in  
 160 dense localization problems (Nehme 2020). CE loss is usually either weighted [51], replaced with a  
 161 Focal loss [52], or applied to a "blobbed" version of the desired boolean volume e.g. by placing a disk  
 162 around each GT position [53–55]. Alternative methods take a soft version of the binary classification  
 163 problem. That is, by placing a small Gaussian around each GT position (e.g. with std of 1 pixel),  
 164 and matching continuous heatmaps, backpropagation yields more meaningful gradients and eases the  
 165 learning process convergence.

166 Localization heatmaps thus form a natural encoding for SMLM images, which can be input to our  
 167 conditional diffusion model. Therefore, to encode raw data  $\mathbf{x}$  into a more tractable representation, we  
 168 train the DeepSTORM architecture (Nehme 2020). Raw coordinates  $\theta$  are binned into an upsampled  
 169 image  $\mathbf{z}$ .

$$\mathcal{L}(\mathbf{y}, \hat{\mathbf{y}}) = \|\mathbf{y} - \hat{\mathbf{y}}\|^2$$

## 170 4 Experiments

171 All training data was simulated under the likelihood and impulse response (2,10), drawing coordinates  
 172 uniformly over a disc with a radius of 7 pixels.

### 173 4.1 Model Precision on Simulated Ensembles

### 174 4.2 Model Uncertainty

175 We set  $T = 100$  for all experiments and treat forward process variances  $\beta_t$  as hyperparameters,  
 176 with a linear schedule from  $\beta_0 = 10^{-4}$  to  $\beta_T = 10^{-2}$ . These constants were chosen to be small  
 177 relative to data scaled to  $[-1, 1]$ , ensuring that reverse and forward processes have approximately  
 178 the same functional form while keeping the signal-to-noise ratio at  $x_T$  as small as possible ( $L_T =$   
 179  $D_{KL}(q(x_T|x_0)\|\mathcal{N}(0, I)) \approx 10^{-5}$  bits per dimension in our experiments).

180 To represent the reverse process, we used the DDPM architecture based on a U-Net backbone (Ho  
 181 2020). Parameters are shared across time, which is specified to the network using the Transformer

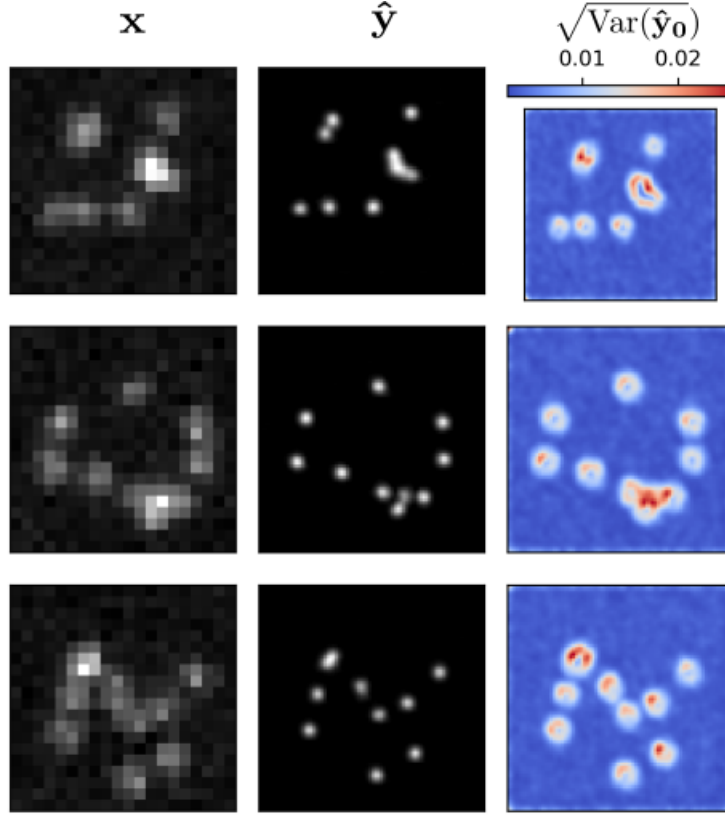


Figure 3: Kernel density estimates for various signal to noise ratios (SNR)

182 sinusoidal position embedding ?. We use self-attention at the  $16 \times 16$  feature map resolution ??.  
 183 Details are in Appendix A.

184 and the channel multipliers at different resolutions (see Appendix A for details). To condition the  
 185 model on the input  $x$ , we up-sample the low-resolution image to the target resolution using bicubic  
 186 interpolation. The result is concatenated with  $y_t$  along the channel dimension. We experimented with  
 187 more sophisticated methods of conditioning, such as using, but we found that the simple concatenation  
 188 yielded similar generation quality.

## 189 5 Related Work

### 190 5.1 Diffusion Models

191 Prior work of diffusion models ?? require 1-2k diffusion steps during inference, making generation  
 192 slow for large target resolution tasks. We adapt techniques from ? to enable more efficient inference.  
 193 Our model conditions on  $\gamma$  directly (vs  $t$  as in ?), which allows us flexibility in choosing the number  
 194 of diffusion steps, and the noise schedule during inference. This has been demonstrated to work  
 195 well for speech synthesis ?, but has not been explored for images. For efficient inference, we set the  
 196 maximum inference budget to 100 diffusion steps, and hyper-parameter search over the inference  
 197 noise schedule. This search is inexpensive as we only need to train the model once ?. We use FID on  
 198 held-out data to choose the best noise schedule, as we found PSNR did not correlate well with image  
 199 quality.

## 6 Conclusion

## References

- [1] Nehme, E., et al. *DeepSTORM3D: dense 3D localization microscopy and PSF design by deep learning*. Nature Methods 17, 734–740 (2020).
- [2] Ouyang, W., et al. *Deep learning massively accelerates super-resolution localization microscopy*. Nature Biotechnology 36, 460–468 (2018).
- [3] Speiser, A., et al. *Deep learning enables fast and dense single-molecule localization with high accuracy*. Nature Methods 18, 1082–1090 (2021).
- [4] Sohl-Dickstein J., et al. *Deep unsupervised learning using nonequilibrium thermodynamics*. ICLR (2015).
- [5] Ho J., et al. *Denoising Diffusion Probabilistic Models*. Advances in Neural Information Processing Systems 2015).
- [6] Nanxin C., et al. *WaveGrad: Estimating Gradients for Waveform Generation*. ICLR (2021).
- [4] Chao, J., et al. *Fisher information theory for parameter estimation in single molecule microscopy: tutorial*. Journal of the Optical Society of America A 33, B36 (2016).
- [5] Schermelleh, L. et al. *Super-resolution microscopy demystified*. Nature Cell Biology vol. 21 72–84 (2019).
- [6] Zhang, B., et al. *Gaussian approximations of fluorescence microscope point-spread function models*. (2007).
- [7] Smith, C.S., *Fast, single-molecule localization that achieves theoretically minimum uncertainty*. Nature Methods 7, 373–375 (2010).
- [8] Nieuwenhuizen, R., et al. *Measuring image resolution in optical nanoscopy*. Nature Methods 10. 557-562 (2013).
- [9] Huang, F., et al. *Video-rate nanoscopy using sCMOS camera-specific single-molecule localization algorithms*. Nat Methods 10, 653–658 (2013).
- [10] Rust, M., et al. *Sub-diffraction-limit imaging by stochastic optical reconstruction microscopy (STORM)*. Nat Methods 3, 793–796 (2006).
- [11] Betzig, E., et al. *Imaging intracellular fluorescent proteins at nanometer resolution*. Science 313, 1642–1645 (2006).
- [12] Weigert, M., et al. *Content-aware image restoration: pushing the limits of fluorescence microscopy*. Nat. Methods 15, 1090 (2018).
- [13] Falk, T., et al. *U-net: deep learning for cell counting, detection, and morphometry*. Nat. Methods 16, 67–70 (2019).
- [14] Boyd, N., et al. *DeepLoco: fast 3D localization microscopy using neural networks*. Preprint at bioRxiv <https://doi.org/10.1101/267096> (2018)
- [15] Zelger, P., et al. *Three-dimensional localization microscopy using deep learning*. Opt. Express 26, 33166–33179 (2018)
- [16] Zhang, P., et al. *Analyzing complex single-molecule emission patterns with deep learning*. Nat. Methods 15, 913 (2018)
- [17] Saharia, C., et al. *Image Super-Resolution via Iterative Refinement*. Preprint at arXiv <https://doi.org/10.48550/arXiv.2104.07636> (2021)
- [18] Kim, T., et al. *Information-rich localization microscopy through machine learning*. Nat Commun 10, 1996 (2019).

## A Appendix

Standard SMLM localization algorithms based on maximum likelihood estimators or least squares optimization require tight control of activation and reactivation to maintain sparse emitters, presenting a tradeoff between imaging speed and labeling density. Recently, deep models have generalized SMLM to densely labeled structures by predicting high-resolution kernel density estimates (KDEs) from low resolution images with convolutional networks. However, estimated KDEs may contain irregularities due to finite sample sizes and limited model capacity.

247 The DeepSTORM CNN, initially proposed in (Nehme 2020) for 3D localization, can be viewed  
 248 as a deep kernel density estimator, reconstructing kernel density estimates  $\mathbf{y}$  from low-resolution  
 249 inputs  $\mathbf{x}$ . We utilize a simplified form of the original architecture for 2D localization, which we  
 250 denote  $\phi$  hereafter, which consists of three main modules: a multi-scale context aggregation module,  
 251 an upsampling module, and a prediction module. For context aggregation, the architecture utilizes  
 252 dilated convolutions to increase the receptive field of each layer. The upsampling module is then  
 253 composed of two consecutive 2x resize-convolutions, computed by nearest-neighbor interpolation,  
 254 to increase the lateral resolution by a factor of 4. For a common sCMOS camera, each pixel has a  
 255 lateral size of approximately 108 nanometers, giving approximately 27 nanometer pixels in the KDE.  
 256 The terminal prediction module contains three additional convolutional blocks for refinement of the  
 257 upsampled image, followed by an element-wise HardTanh.

258 Single molecule localization microscopy (SMLM) relies on the temporal resolution of fluorophores  
 259 whose spatially overlapping point spread functions would otherwise render them unresolvable  
 260 at the detector. Common strategies for the temporal separation of molecules involve molecular  
 261 photoswitching from dark to fluorescent states, permitting resolution of fluorophores beyond the  
 262 diffraction limit. Estimation of molecular coordinates is typically carried out by modeling the optical  
 263 impulse response of the imaging system and fitting model functions to the data. However, such  
 264 models are only well-suited to isolated molecules, reducing the number of molecules in the field of  
 265 view and limiting temporal resolution in super resolution microscopy. This issue has incited a series  
 266 of efforts to increase the density of fluorescent molecules imaged in a single frame while developing  
 267 appropriate models for dense localization.

268 In fluorescence microscopy, each pixel is treated as a Poisson random variable (Smith 2010; Nehme  
 269 2020; Chao 2016), with expected value

$$\omega = i_0 \int O(u) du \int O(v) dv \quad (10)$$

270 where  $i_0 = \eta N_0 \Delta$ . The scalar parameters  $\eta, \Delta$  are the photon detection probability of the sensor and  
 271 the exposure time, respectively. Without loss of generality, we assume  $\eta = \Delta = 1$ . Most importantly,  
 272  $N_0$  represents the signal amplitude, which we assume maintains a fixed value. The optical impulse  
 273 response  $O(u, v)$  is often approximated as a 2D isotropic Gaussian with standard deviation  $\sigma$  (Zhang  
 274 2007). This approximation has the convenient property, that the effects of pixelation can be expressed  
 275 in terms of error functions. For example, given a fluorescent emitter located at  $\theta = (u_0, v_0)$ , we have  
 276 that

$$\int O(u) du = \frac{1}{2} \left( \operatorname{erf} \left( \frac{u_k + \frac{1}{2} - u_0}{\sqrt{2}\sigma} \right) - \operatorname{erf} \left( \frac{u_k - \frac{1}{2} - u_0}{\sqrt{2}\sigma} \right) \right) \quad (11)$$

277 where we have used the common definition  $\operatorname{erf}(z) = \frac{2}{\sqrt{\pi}} \int_0^t e^{-t^2} dt$ . Our generative model also  
 278 incorporates a normally distributed white noise per pixel  $\zeta$  with offset  $o$  and variance  $\sigma^2$ . Ultimately,  
 279 we have a Poisson component of the signal, which scales with  $N_0$  and a Gaussian component, which  
 280 does not.

281 Consider,

$$\zeta_k - o_k + \sigma_k^2 \sim \mathcal{N}(\sigma_k^2, \sigma_k^2) \approx \text{Poisson}(\sigma_k^2) \quad (12)$$

282 Since  $\mathbf{x}_k = \mathbf{s}_k + \zeta_k$ , we transform  $\mathbf{x}'_k = \mathbf{x}_k - o_k + \sigma_k^2$ , which is distributed according to

283 Consider the factorization  $p(\hat{\mathbf{y}}|\mathbf{x}, \mathbf{y})p(\mathbf{x}|\mathbf{y})p(\mathbf{y}) = p(\mathbf{x}|\mathbf{y}, \hat{\mathbf{y}})p(\mathbf{y}|\hat{\mathbf{y}})p(\hat{\mathbf{y}})$ . Given that  $\mathbf{x}$  is condition-  
 284 ally independent of  $\hat{\mathbf{y}}$ , we find

$$p_{\Psi}(\hat{\mathbf{y}}|\mathbf{x}, \mathbf{y}) = p(\mathbf{y}|\hat{\mathbf{y}})$$



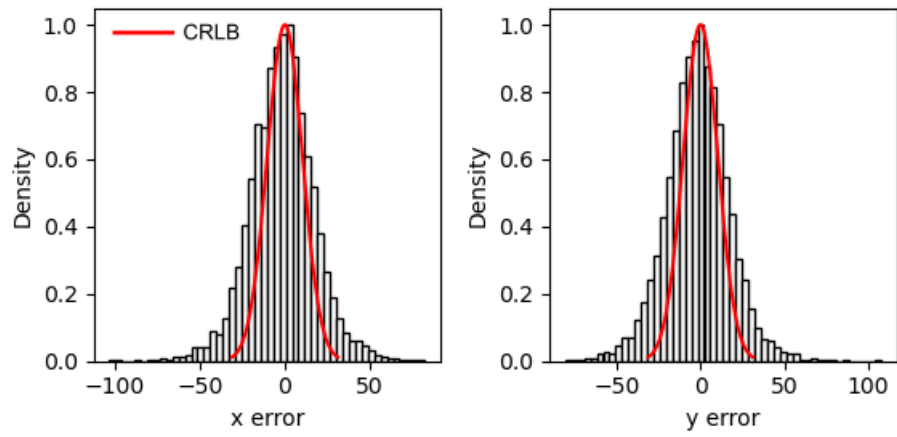


Figure 4: Localization errors of the trained model